A laboratory model for iron snow in planetary cores

Ludovic Huguet, Michael Le Bars, Renaud Deguen

A laboratory model for iron snow in planetary cores

Ludovic Huguet[1,2], Michael Le Bars[2], Renaud Deguen[1]

[11] ISTerre, Université Grenoble Alpes, Université Savoie Mont Blanc, CNRS, IRD, Université Gustave Eiffel, 38000 Grenoble, France
[22] CNRS, Aix Marseille Univ, Centrale Marseille, IRPHE, Marseille, France

Key Points:

- We have carried out an experimental study of the dynamics of iron snow.
- Our experiments present crystallization cycles, with intense solidification bursts separated by quiet periods.
- This cyclic pattern is controlled by thermal diffusion and by the amount of supercooling required for crystallization.

Corresponding author: Ludovic Huguet, `ludovic.huguet@univ-grenoble-alpes.fr`

Abstract

Solidification of the cores of small planets and moons is thought to occur in the 'iron snow' regime, in which iron crystals form near the core-mantle boundary and fall until re-melting at higher depth. The resulting buoyancy flux may sustain convection and dynamo action. This regime is poorly known, having never been observed in the field or laboratory. Here we present the first laboratory experiments designed to model iron snow. We find that solidification happens in a cyclic pattern, with intense solidification bursts separated by crystal-free periods. This is explained by the necessity of reaching a finite amount of supercooling to re-initiate crystallization once the crystals formed earlier have migrated away. When transposed to planetary cores, our results suggest that crystallization and the associated buoyancy flux would be strongly heterogeneous in time and space, which eventually impacts the time variability and geometry of the magnetic field.

Plain Language Summary

In small planets or moons with iron core, solidification proceeds from the top down, producing solid iron crystals at the top of the core. These crystals then fall down until they melt at deeper depth, where the temperature is larger. By analogy with snow in the atmosphere, this regime is called iron snow. It creates motions in the liquid core and provides energy for generating a magnetic field. But the key aspects of this regime remain largely unknown. Using analog laboratory experiments, we have found that solidification happens in a cyclic pattern, with periods of intense crystal formation followed by quiet periods with no crystals. This happens because crystallization needs a certain amount of cooling below the solidification temperature to be triggered, while all crystals have raised and melt. Applied to planetary cores, it means that the iron snow would be heterogeneous in space and time, with intermittent and localized crystal falling. This would affect the shape and strength of the planet's magnetic field.

1 Introduction

Solidification of planetary cores starts when and where the temperature first drops below the solidification temperature. Depending on the pressure range and core composition, the slope of the melting curve can be steeper or shallower than the actual temperature profile (Williams, 2009), which implies that solidification may start either at the planet's center (as for Earth (Jacobs, 1953)), near the core-mantle boundary (CMB) (as for Moon (Jing et al., 2014), Ganymede (Hauck et al., 2006; Rückriemen et al., 2015), Mercury (Vilim et al., 2010; Chen et al., 2008; Dumberry & Rivoldini, 2015; Edgington et al., 2019), Mars (Stewart et al., 2007; Davies & Pommier, 2018), metallic asteroids (Scheinberg et al., 2016)), or at multiple core locations (as for Mercury (Chen et al., 2008; Dumberry & Rivoldini, 2015)).

In the situation where the solidification temperature is reached first at the CMB, solidification is thought to occur in the so-called "iron snow" regime, in which free iron crystals form near the CMB and fall until re-melting in a hotter, deeper region (Hauck et al., 2006). Solidification and melting affect the composition profile, and this is thought to result in a core structure consisting in a stably stratified layer near the CMB, where buoyantly unstable iron crystals crystallize and fall (i.e. the snow zone), and a deeper, convective layer with temperatures above the liquidus (Fig. 1a). The melting of crystals beneath the stratified layer provides a source of buoyancy for compositional convection (Breuer et al., 2015; Davies & Pommier, 2018), which can generate a magnetic field through dynamo action (Christensen, 2006, 2015).

The modeling of this scenario (Hauck et al., 2006; Davies & Pommier, 2018) relies on important assumptions: (i) the snow layer is in thermodynamic equilibrium, (ii) solid iron rapidly sinks and remelts (compared to the cooling rate) beneath the snow layer,

and (iii) crystallization and sinking of iron crystals do not lead to radial mixing, resulting in compositional layering. A more general model allowing, for example, thermodynamic disequilibrium would require parameterization of all small-scale effects, which are still poorly understood (Loper, 1992). In addition, the interaction between reactive particles (Huguet et al., 2020) and a stratified layer, as well as the collective behavior of iron crystals (Kriaa et al., 2022) and their effects on large-scale flow, can alter the picture of steady iron snow. While the heterogeneity of the flux at the core upper boundary (Amit et al., 2015) or the radial distribution of the buoyancy flux (Cao et al., 2014) modify the resulting magnetic field, dynamo simulations driven by iron snow have so far assumed a uniform and stationary buoyancy flux below the snow layer (Vilim et al., 2010; Christensen, 2015).

Current models of core crystallization neglect any nucleation barrier. Yet, the supercooling required for crystal nucleation could be of several hundred kelvins (Huguet, Van Orman, et al., 2018; Davies et al., 2019; Wilson et al., 2021; Sun et al., 2021; Wilson et al., 2023). In the case of top-down crystallization, heterogeneous nucleation at the CMB could help reduce the nucleation barrier. The detachment of iron crystals from the CMB could then provide nucleation sites in the bulk and allow the development of iron snow (Huguet, Hauck, et al., 2018; Neufeld et al., 2019). However, geodynamic studies (Hauck et al., 2006; Davies & Pommier, 2018) have focused on the bulk production of crystals in a quasi-steady and equilibrium state.

Here, we present results from laboratory experiments that include the key ingredients of the "iron snow" — crystallization of free crystals, sedimentation, and re-melting. Experimental results and modeling allow us to understand the dynamics of this regime. We then discuss potential consequences on the evolution of planetary cores and magnetic field.

2 Experimental setup

Fig. 1(b,c) show schematics of our experimental setup. It is an upside-down version of iron snow crystallization, using water as an analog for the metal core: less dense ice crystals rise and melt above the liquidus, releasing fresh water. In a tank of $32\times32\times$ 20 cm, we have poured about 17 liters of distilled water, and slowly injected at the bottom between 3 and 4 liters of salty water with a concentration of 24% (green area in Fig. 1b,c). This salty layer, with a low solidification temperature, avoids direct contact between the freshwater and the cold lower boundary, which would otherwise lead to strong cohesive forces between the ice and the cooled boundary. The tank has been carefully sealed with a 2 cm thick transparent plexiglass sheet (experiment (a)) or copper plate (experiment (b)). The top boundary and walls are insulated from the outside (which is about 25°C) with polystyrene sheets, except on the front and rear sides. The bottom boundary consists of a chrome-plated copper plate 3 cm thick and its temperature is set at about −18°C. After a few days of cooling from below, the first crystallization either occurs spontaneously or is triggered by the insertion of a metal rod at the bottom of the tank.

We monitored the temperature at both boundaries and the evolution of the dynamics of crystallization with several cameras. We used a Point-Grey camera at 1 frame per second from the front of the experiments. Diffusive backlighting has been used to illuminate the tank at the rear of the experiment. A 1 W green laser has been used to create a horizontal (or vertical) laser plane at mid-height (or mid-width) in the tank. We visualized the ice crystals crossing the laser sheet by using a Nikon D80 recording video at 30 frames per second from above through the transparent top boundary (only for experiments (a)). With a vertical plane, PIV measurements have been performed in some of our experiments before the first crystallization. Note that the PIV particles we used do not affect the crystallization, as they do not act as nucleation sites.

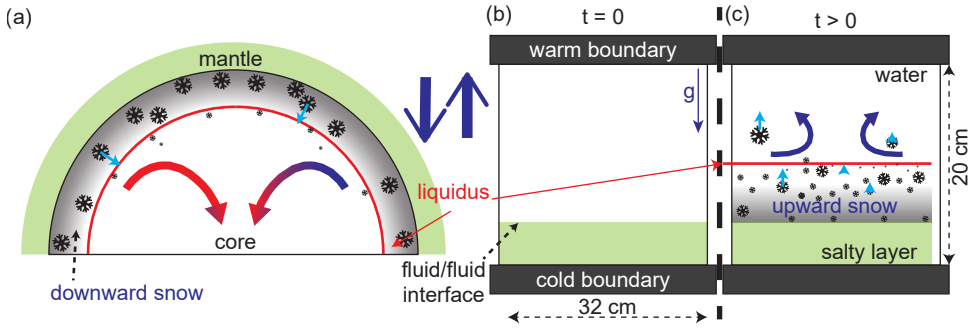

Figure 1. (a) Schematic view of an iron snow regime in a planetary core. Iron crystals solidify in the liquid bulk close to the core-mantle boundary, and settle into the hotter and deeper part of the liquid core, where they melt. It induces compositional convection due to the release of an iron-rich melt. Note that the experiments are upside-down compared to the core (blue arrows). (b) Experimental setup at $t = 0$. The tank is cooled from below. The bottom salty layer (green) prevents the crystals from attaching to the bottom surface. (c) At $t > 0$, free crystals grow in a supercooled layer between the fluid/fluid interface and the liquidus isotherm. The buoyant crystals settle toward the top of the tank and melt once reaching the liquidus. The gray gradient zone indicates a slight salt stratification because of salt diffusion from the bottom layer.

3 Results

3.1 Description of the dynamics in the experiments

The evolution of the experiments consists of successive periods of crystallization, thereafter called burst, separated by quiescent periods without crystallization. Fig. 2a shows the horizontal average of the pixel intensity of images obtained with the front camera, as a function of time and depth in the tank. The presence of crystals decreasing the pixels' intensity, this gives a qualitative measure of the amount of suspended crystals. Here, each vertical gray strike corresponds to a burst of crystallization. We understand each cycle as follows. (1) Heat is removed through diffusion through the bottom boundary of the tank, resulting in the gradual cooling of the lower part of the tank and the supercooling of a layer at intermediate depth; this supercooled layer does not extend down to the bottom of the tank due to the presence of salt which acts as an antifreeze. (2) When the amount of supercooling exceeds some threshold, crystals nucleate in the supercooled layer. Crystallization releases latent heat which increases the temperature up to the liquidus, thus restoring thermodynamic equilibrium. (3) The buoyant ice crystals migrate upward and remelt when they reach a height at which the water temperature exceeds 0°C. Melting acts as a heat sink, decreasing the temperature at which the crystals melt. (4) The supercooling is partly suppressed by the latent heat released. In addition, cold water entrained by rising crystals is replaced by hotter water from above. As all nucleation sites have been removed, the burst of crystallization ends.

These cycles repeat periodically with a period τ (duration of the crystallization bursts plus quiet period) which is about 1440 s $\pm$400 s and 1490 s $\pm$750 s for the experiments (a, b) (Fig. 2b). The large variability in the period might be due to the stochastic nature of the nucleation, i.e., the nucleation initiation strongly depends on the presence of heterogeneous nucleation sites. The upper boundary of the snow region is the height where ice crystals remelt. In Fig. 2a (black dashed line), the highest height reached after each burst by the buoyant ice crystals increases roughly linearly with time, at a rate $V \simeq 2(\pm 0.5) \times 10^{-6}$ m.s^{-1}.

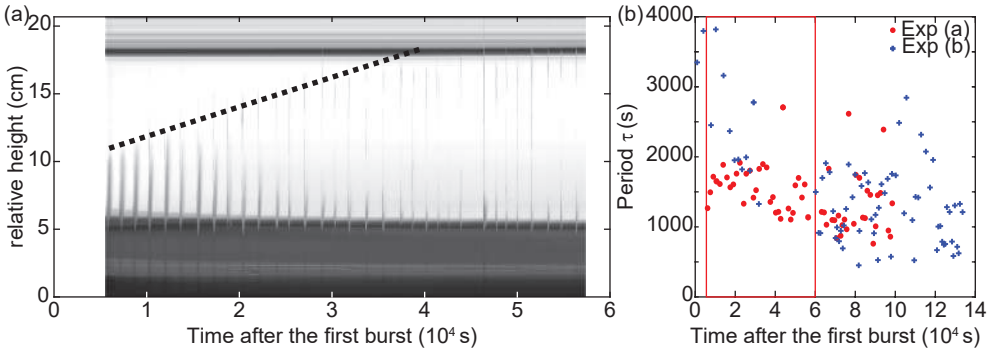

Figure 2. (a) Spatio-temporal diagram as a function of height and time after the first burst for experiment (a) (see Supporting Information Fig. S1(a) for temperature evolution). The dotted black line shows approximately the top boundary of the snow layer (about 0°C). The bursts of crystallization correspond to the dark vertical stripes interposed between quiet periods. (b) Evolution of the time interval between two bursts during two experiments (red dots and blue crosses). The red rectangle denotes the duration of the spatio-temporal diagram in (a).

Fig. 3 illustrates the sequence of one burst of crystallization. Nucleation occurs close to the fluid/fluid interface (and to the walls) where supercooling is the largest and heterogeneity might ease ice crystal nucleation (blue box in the first image of Fig. 3). In a few hundred seconds, the crystallization propagates through the supercooled layer. The propagation of the nucleation events may be explained by collisional breeding, which corresponds to the breaking of ice crystals into tiny particles due to their collisions during the advection (Svensson & Omstedt, 1994), which provides new nucleation sites in the supercooled layer. Here the advection is due to the positive buoyancy of the ice crystals. This phenomenon has been described for the crystallization of frazil-ice, which is formed in sea ice or supercooled river (Svensson & Omstedt, 1994; Rees Jones & Wells, 2018). Ice crystals rapidly grow and form almost 2D crystals, so-called platelet ice crystals. The smallest crystals rise slowly and melt almost instantly when crossing the liquidus. On the contrary, the larger ones have a larger velocity (see Supporting Information Fig. S2) and can overshoot the liquidus and melt at higher heights (dotted dashed line in Fig. 3).

3.2 Diffusive model and heat budget

This sequence of crystallization results in a layered structure consisting of a lower layer with a diffusive temperature profile in which the crystallization bursts occur, an intermediate layer at a temperature near 0°C produced by the remelting of the ice crystals, and an upper layer in which the temperature gradually increases from 0°C to T_{top} at the upper boundary of the tank (see Fig. 4b). We developed a 1D model for temperature and chemical evolution using the two diffusion equations with $\kappa = 1.4{\times}10^{-7}$ m^2 s^{-1} and $D = 1 \times 10^{-9}$ m^2 s^{-1} for the thermal and chemical diffusivities, respectively. We solved the diffusion equations using a no-flux boundary condition for the composition and set the temperature at each boundary to be equal to the time-dependent temperatures measured in the experiments (see Supporting Information Fig. S1 for temperature evolution). Note that due to the maximum density of water around 4° C, which depends on the salt concentration, a layer with an unstable gradient exists (white area in Fig. 4b). Our diffusive model and PIV measurements before the crystallization (see Supporting Information Fig. S4) show that the convective layer translates toward the top of the tank due to the increase of the salt concentration above the salty layer, which sup-

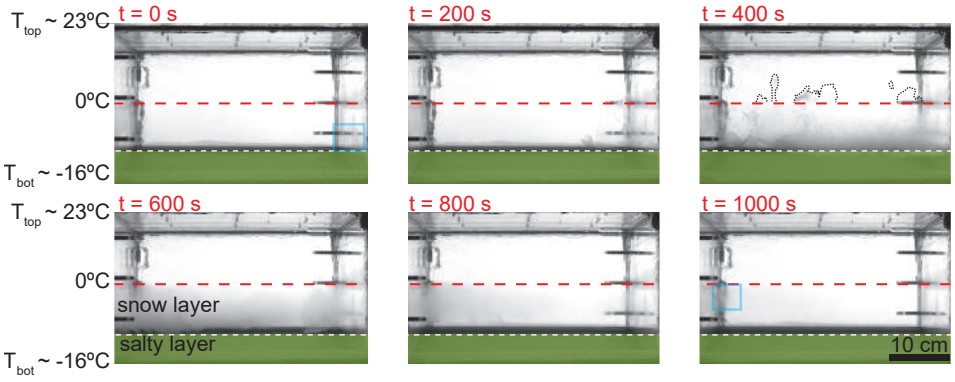

Figure 3. Timeline of a burst crystallization. The crystallization phase starts along the right wall (blue box on the top-left picture) and ends when the last crystals melt while passing through the liquidus (blue box on the bottom-right row). The dotted black lines at $t = 400$ s denote the overshoot due to the presence of large crystals which have a rising velocity larger than the melting rate. This burst crystallization lasts about 1000 s. The white dashed line shows the top of the salty layer. The red line denotes the liquidus isotherm (0°C), based on the diffusive model developed below.

presses the unstable gradient. Our measured concentration profile at the end of the experiments shows that salt concentration is higher than predicted by the diffusive model (see Supporting Information Fig. S3), meaning that bursts of crystallization mix the salt into the top layer, which may suppress the convection layer. Fig. 4a shows the temperature evolution in the tank. After the first crystallization burst (red vertical line), the temperature and concentration profiles might be altered by the crystallization bursts, as they are not considered in our model. The position of the liquidus is well predicted by our model (about 11 cm height in Fig. 2a at the time of the first burst). Our model also predicts a significant supercooling of 6° C for the first burst, which agrees with the observation of a massive event of crystallization for the initial burst.

To estimate the amount of supercooling during a quiescent period and the maximum quantity of ice crystal formed by a burst, we use the modeled temperature and concentration profiles at $t \sim 184000$ s (first burst of the experiment (a)). Then, we set the temperature at the liquidus in the supercooled layer, assuming that the first burst has reinstalled thermal equilibrium (see solid black line in Fig. 4b). We then run our diffusive model and show the temperature profile after $\tau = 1500$ s. The supercooled layer is about 6 cm thick and the maximum supercooling is about 1.5° C (Fig. 4b). The energy $E_{burst} = \rho c_p \int_0^H (T_m - T) dz \simeq 290 \times 10^3$ J m^{-2} for $(T < T_m)$ stored in this layer would be converted to ice crystals once nucleation is initiated (gold area in Fig. 4b).

Our qualitative understanding can be tested by considering the energy balance during one cycle. Since all the crystals produced during a burst remelt before the next cycle, there is no contribution of latent heat to the energy budget when integrated over a period τ. It reduces to a balance between the change in internal energy and the amount of energy extracted from the tank. According to our thermal diffusion model, the amount of energy extracted from the bottom and injected from the top are $\Delta E_b = k \int_0^\tau \frac{\partial T}{\partial z}\big|_b \, dt \simeq 250 \times 10^3$ J m^{-2} and $\Delta E_t = k \int_0^\tau \frac{\partial T}{\partial z}\big|_t \, dt \simeq 80 \times 10^3$ J m^{-2}, respectively, with a net extracted energy $\Delta E \simeq 170 \times 10^3$ J m^{-2}. We can indirectly estimate the change in internal energy from the evolution of the melting front, which migrates upward at a velocity V (Fig. 2). Since it materializes the 0°C isotherm, its migration must be associ-

ated with net cooling of the upper part of the tank. This should be the only significant source of change of internal energy because the temperature in the lower part of the tank is reset to the liquidus after each burst. Assuming that the temperature profile above the melting front is in a near steady state in a reference frame traveling with the boundary, then moving the 0°C isotherm by a distance $\delta h = V\tau$ comes down to replacing a layer of thickness δh at temperature T_{top} by a layer of the same thickness at temperature 0°C. The associated change of internal energy is $\delta h \rho c_p (T_{top} - 0°) \simeq 150 \times 10^3$ J m^{-2}, which is indeed close to the energy ΔE extracted from the tank during a cycle.

The energy released in the form of latent heat during a burst, $E_{burst} \simeq 290 \times 10^3$ J m^{-2}, is close to the energy extracted from the bottom, $\Delta E_b \simeq 250 \times 10^3$ J.m^{-2}. This is consistent with the idea that the evolution of the supercooling is controlled by diffusive cooling from the bottom. Note that although latent heat does not appear in the time-integrated energy budget, the freezing/melting process plays an important role in transporting energy between the lower and upper parts of the tank.

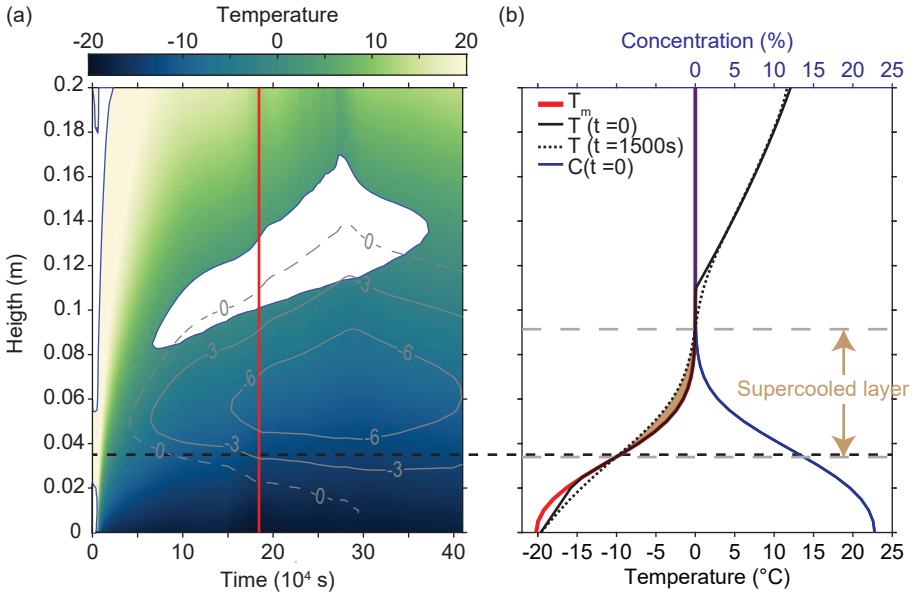

Figure 4. (a) Temperature evolution is shown from the beginning of the experiment to the end. The vertical red line denotes the first crystallization event after $\sim$ 2 days. The white area denotes the zone where the density gradient is unstable because of water specific equation of state (negative thermal expansion coefficient below 4°C, depending on the salt content). The dashed, and solid gray lines denote the liquidus and isolevel of the degree of supercooling, respectively. The dashed black line shows the initial thickness of the salty layer. (b) Temperature (red, black dashed, and solid lines; bottom x-axis) and concentration profile (blue line; top x-axis) as a function of height. The temperature profile evolves from the solid black line ($t = 0$ s after the first burst, i.e., the vertical red line in (a)) with a temperature equal to the liquidus in the snow layer. The black dashed line is the temperature profile after 1500 s, just before a burst event. The gold area is the amount of supercooling after a cooling period.

3.3 Crystal size distribution

We observed a wide range of sizes of crystals (between sub-millimeter to a few centimeters) and we measured the crystal size distribution by analyzing images from above.

For experiment (a), we analyzed 2 hours of video spanned over 7 hours, in which 8 bursts of crystallization occurs. By measuring the area of each crystal crossing the laser sheet over time, we have measured the distribution of the effective radius $r \sim \sqrt{S/\pi}$ (with S, the measured area). Most of the incertitude concerns the smallest crystal radii (left side of the PDF, below 4×10^{-4} m in Fig. 5). However, the overall shape of the PDF is not affected by the threshold criterion used in the image analysis. Fig. 5a shows the probability density function (PDF) of the effective crystal radius. The distribution is well explained by a power law as $\mathrm{PDF}(r) \propto r^{-D-1}$, where $D = 1.6$ is the fractal dimension (Turcotte, 1997) (Fig. 5a). The fractal dimension being smaller than 2, the largest crystals dominate the total surface area of the crystals crossing the laser sheet (Turcotte, 1997), even though most of the crystals have sub-millimeter radius.

We estimate the mass flux of ice crystals (Fig. 5b) using the following relationship between the effective radius and rising velocity of the crystals:

$$U = \sqrt{\frac{8rg\Delta\rho}{3\rho C_d}}, \tag{1}$$

where r, g, ρ, and $\Delta\rho$ are the radius, gravity, water density, and the difference of density between ice and water. The drag coefficient C_d is a function of the Reynolds number (Clift et al., 1978). We assume that the complex shapes of the crystals and the interaction between them do not change significantly the drag coefficient. Despite uncertainty in the velocity/radius relationship, we think that the shape of the distribution of mass flux is significant. As the largest crystals contribute more to the total area, they also contribute more to the total mass flux as they rise faster. The relatively wide range of crystal size (which may be limited by the size of the tank and the camera resolution) might lead to a complex two-way coupling between fluid and solid particles, meaning that fluid flow might impact smaller particles' behavior while larger ones might impact the large-scale flow (Balachandar & Eaton, 2010; Brandt & Coletti, 2022). The interactions between fluid and solid particles will depend on their size distribution and solid fraction (Harada et al., 2012), but also on the state of the environment: stratified or uniform (Deepwell & Sutherland, 2022). Therefore, assuming a single size of crystals is not realistic to model iron snow in planetary cores.

4 Discussion

Our experiments suggest that crystallization in the core of small planets may proceed as crystallization bursts in a supercooled, stably stratified layer below the CMB. These bursts would lead to a wide range of iron crystal sizes. If the core is stably stratified below the CMB (owing to the release of light elements during previous crystallization events or to a subadiabatic temperature profile), then the evolution of its temperature is controlled solely by heat diffusion and the cooling rate, which is set by the heat flux at the CMB q_{CMB}. In this situation, starting at a given time $t = 0$ from a temperature in the vicinity of the CMB equal to the liquidus, the thickness δ of the supercooled layer increases with time t as $\delta \sim \sqrt{\kappa t}$, while the supercooling ΔT at the CMB increases as (Carslaw & Jaeger, 1986)

$$\Delta T(t) = \frac{q_{CMB}}{k}\sqrt{\frac{4\kappa}{\pi}}t^{\frac{1}{2}}, \tag{2}$$

where k and κ are the thermal conductivity and diffusivity of liquid iron, respectively. Applied to a small planetary core (as Mars (Davies & Pommier, 2018) or Ganymede (Rückriemen et al., 2015)) with the typical values $q_{CMB} \sim 10\ \mathrm{mW\,m^{-2}}$, $k = 40\ \mathrm{W\,m^{-1}\,K^{-1}}$, and $\kappa = 8{\times}10^{-6}\ \mathrm{m^2\,s^{-1}}$, equation 2 predicts that a supercooling of 0.1 K, 1 K, 10 K would be built in 500 yr, 50 kyr, and 5 Myr, respectively. The corresponding thicknesses of the supercooled layer are about 0.3 km, 3 km, 30 km, respectively. The supercooling required

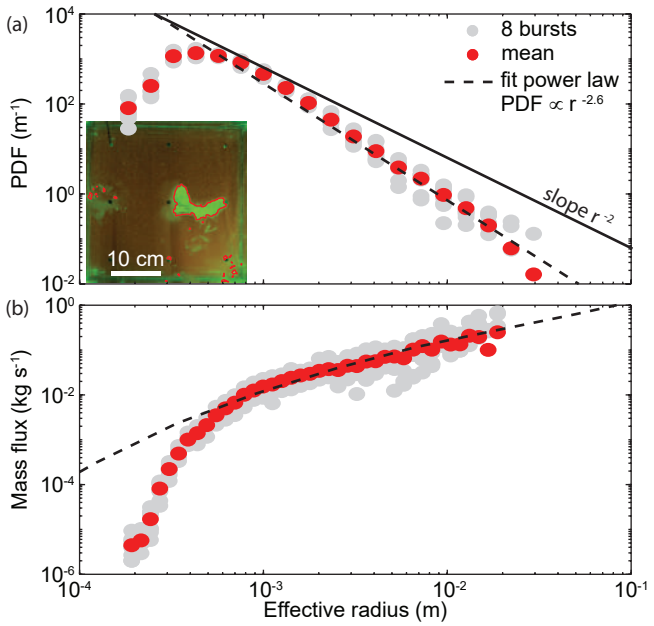

Figure 5. (a) Probability density function (PDF) of crystal effective radius. Gray and red dots denote the 8 bursts and the mean of the distribution, respectively. The black dashed line is a fit of a power law. (b) Estimated mass flux during a crystallization burst as function of the effective radius. Insert in (a) correspond to a top-view snapshot of the detected crystals (red outline) crossing the laser plane.

to nucleate crystals in this layer is not known: homogeneous nucleation requires a supercooling of possibly a few hundred of Kelvin (Huguet, Van Orman, et al., 2018; Sun et al., 2021; Wilson et al., 2023), but the presence of nucleation sites could decrease it by several orders of magnitude. We can note, however, that the time needed to initiate a crystallization burst exceeds the magnetic diffusive timescale ($\sim$ 10 kyr) if the required supercooling is larger than $\simeq$ 0.5 K. In this situation, an iron snow regime with such sparse crystallization bursts might result in intermittent convection and dynamo action, with periods of low and high-intensity magnetic field. On the other hand, negligible supercooling is plausible if iron crystals are attached to the CMB, which might provide nucleation sites. This scenario may lead to the crystallization of large iron crystals, which will be detached by delamination of the crystal layer (Neufeld et al., 2019) or necking of iron dendrites (Huguet, Hauck, et al., 2018). These mechanisms would also imply variability of the crystal flux in space and time.

On Earth, the large heterogeneity of heat flux at the CMB affects the geodynamo and the geomagnetic field (Olson, 2016; Nakagawa, 2020; Sahoo & Sreenivasan, 2020). On Mars, a strongly localized heat flux may explain the extinction of the magnetic field (Sreenivasan & Jellinek, 2012; Amit et al., 2015). Similarly, a heterogeneous "iron snow" regime likely impacts the core dynamics. However, the outcome in terms of magnetic field structure or intensity remains to be investigated. In the future, new simulations are required to model snow experiments. This will require parameterizing the formation and melting of crystals, including the statistical aspect of nucleation.

5 Open Research Section

The numerical code used in this work is written in Matlab. Code and data to reproduce the figures are available here: `https://figshare.com/s/67fb2c6fc793db90b9c0` with a pre-allocated DOI `dx.doi.org/10.6084/m9.figshare.24056916`. The color map, used in this study, prevent visual distortion of the data and exclusion of readers with color vision deficiencies (Crameri et al., 2020). PIV calculation has been performed using PIVlab Tool for MATLAB (Thielicke & Sonntag, 2021).

Acknowledgments

This work was supported by the European Research Council (ERC) under the European Union's Horizon 2020 research and innovation programme (grant numbers 681835 and 716429). L.H. and M.LB designed the project. L.H. has carried out the experiments and performed the image and data analysis and modeling. All authors discussed the results and reviewed the manuscript. The authors declare that they have no competing financial interests.

References

Amit, H., Choblet, G., Olson, P., Monteux, J., Deschamps, F., Langlais, B., & Tobie, G. (2015). Towards more realistic core-mantle boundary heat flux patterns: a source of diversity in planetary dynamos. *Prog. Earth Planet. Sci.*, *2*(1), 1–26.

Balachandar, S., & Eaton, J. K. (2010). Turbulent dispersed multiphase flow. *Annual review of fluid mechanics*, *42*, 111–133.

Brandt, L., & Coletti, F. (2022). Particle-laden turbulence: progress and perspectives. *Annual Review of Fluid Mechanics*, *54*, 159–189.

Breuer, D., Rueckriemen, T., & Spohn, T. (2015). Iron snow, crystal floats, and inner-core growth: modes of core solidification and implications for dynamos in terrestrial planets and moons. *Progress in Earth and Planetary Science*, *2*(1), 39.

Cao, H., Aurnou, J. M., Wicht, J., Dietrich, W., Soderlund, K. M., & Russell, C. T. (2014). A dynamo explanation for Mercury's anomalous magnetic field. *Geophysical Research Letters*, *41*(12), 4127-4134. doi: 10.1002/2014GL060196

Carslaw, H., & Jaeger, J. (1986). *Conduction of heat in solids. 2nde edition.* Clarendo Press.

Chen, B., Li, J., & Hauck, S. A. (2008). Non-ideal liquidus curve in the Fe-S system and Mercury's snowing core. *Geophysical Research Letters*, *35*(7).

Christensen, U. R. (2006). A deep dynamo generating Mercury's magnetic field. *Nature*, *444*(7122), 1056.

Christensen, U. R. (2015). Iron snow dynamo models for Ganymede. *Icarus*, *247*, 248-259.

Clift, R., Grace, J. R., & Weber, M. E. (1978). *Bubbles, drops, and particles.* Courier Corporation.

Crameri, F., Shephard, G. E., & Heron, P. J. (2020). The misuse of colour in science communication. *Nature communications*, *11*(1), 5444.

Davies, C. J., & Pommier, A. (2018). Iron snow in the martian core? *Earth and Planetary Science Letters*, *481*, 189–200.

Davies, C. J., Pozzo, M., & Alfè, D. (2019). Assessing the inner core nucleation paradox with atomic-scale simulations. *Earth and Planetary Science Letters*, *507*, 1–9.

Deepwell, D., & Sutherland, B. R. (2022). Cluster formation during particle settling in stratified fluid. *Physical Review Fluids*, *7*(1), 014302.

Dumberry, M., & Rivoldini, A. (2015). Mercury's inner core size and core-crystallization regime. *Icarus*, *248*, 254-268.

Edgington, A., Vočadlo, L., Stixrude, L., Wood, I., Dobson, D., & Holmström, E. (2019). The top-down crystallisation of mercury's core. *Earth and Planetary Science Letters*, *528*, 115838.

Harada, S., Mitsui, T., & Sato, K. (2012). Particle-like and fluid-like settling of a stratified suspension. *The European Physical Journal E*, *35*(1), 1.

Hauck, S. A., Aurnou, J. M., & Dombard, A. J. (2006). Sulfur's impact on core evolution and magnetic field generation on Ganymede. *Journal of Geophysical Research*, *111*(E9), 2156-2202. doi: 10.1029/2005je002557

Huguet, L., Barge-Zwick, V., & Le Bars, M. (2020). Dynamics of a reactive spherical particle falling in a linearly stratified fluid. *Physical Review Fluids*(under review).

Huguet, L., Hauck, S., Van Orman, J., & Jing, Z. (2018). Implications of the homogeneous nucleation barrier for top-down crystallization in mercury's core. In *Mercury: Current and future science of the innermost planet* (Vol. 2047, p. 6101).

Huguet, L., Van Orman, J. A., Hauck, S. A., & Willard, M. A. (2018). Earth's inner core nucleation paradox. *Earth and Planetary Science Letters*, *487*, 9–20.

Jacobs, J. A. (1953). The Earth's Inner Core. *Nature*, *172*(4372), 297-298. doi: 10.1038/172297a0

Jing, Z., Wang, Y., Kono, Y., Yu, T., Sakamaki, T., Park, C., ... Shen, G. (2014). Sound velocity of Fe-S liquids at high pressure: Implications for the Moon's molten outer core. *Earth and Planetary Science Letters*, *396*, 78-87.

Kriaa, Q., Subra, E., Favier, B., & Le Bars, M. (2022). Effects of particle size and background rotation on the settling of particle clouds. *Physical Review Fluids*, *7*(12), 124302.

Loper, D. (1992). A nonequilibrium theory of a slurry. *Continuum Mechanics and Thermodynamics*, *4*(3), 213–245.

Nakagawa, T. (2020). A coupled core-mantle evolution: review and future prospects. *Progress in Earth and Planetary Science*, *7*(1), 1–17.

Neufeld, J. A., Bryson, J. F., & Nimmo, F. (2019). The top-down solidification of iron asteroids driving dynamo evolution. *Journal of Geophysical Research: Planets*, *124*(5), 1331–1356.

Olson, P. (2016). Mantle control of the geodynamo: Consequences of top-down regulation. *Geochemistry, Geophysics, Geosystems*, *17*(5), 1935–1956.

Rees Jones, D. W., & Wells, A. J. (2018). Frazil-ice growth rate and dynamics in mixed layers and sub-ice-shelf plumes. *The Cryosphere*, *12*(1), 25–38.

Rückriemen, T., Breuer, D., & Spohn, T. (2015). The Fe snow regime in Ganymede's core: A deep-seated dynamo below a stable snow zone. *Journal of Geophysical Research*, n/a-n/a. (2014JE004781) doi: 10.1002/2014JE004781

Sahoo, S., & Sreenivasan, B. (2020). Response of earth's magnetic field to large lower mantle heterogeneity. *Earth and Planetary Science Letters*, *549*, 116507.

Scheinberg, A., Elkins-Tanton, L. T., Schubert, G., & Bercovici, D. (2016). Core solidification and dynamo evolution in a mantle-stripped planetesimal. *Journal of Geophysical Research*, *121*(1), 2-20. doi: 10.1002/2015JE004843

Sreenivasan, B., & Jellinek, A. M. (2012). Did the tharsis plume terminate the martian dynamo? *Earth and Planetary Science Letters*, *349*, 209–217.

Stewart, A. J., Schmidt, M. W., van Westrenen, W., & Liebske, C. (2007). Mars: A new core-crystallization regime. *Science*, *316*(5829), 1323-1325.

Sun, Y., Zhang, F., Mendelev, M. I., Wentzcovitch, R. M., & Ho, K.-M. (2021). Two-step nucleation of the earth's inner core. *arXiv*.

Svensson, U., & Omstedt, A. (1994). Simulation of supercooling and size distribution in frazil ice dynamics. *Cold regions science and technology*, *22*(3), 221–233.

Thielicke, W., & Sonntag, R. (2021). Particle image velocimetry for matlab: Accuracy and enhanced algorithms in pivlab. *Journal of Open Research Software*,

9(1).

Turcotte, D. L. (1997). *Fractals and chaos in geology and geophysics.* Cambridge university press.

Vilim, R., Stanley, S., & Hauck, S. (2010). Iron snow zones as a mechanism for generating Mercury's weak observed magnetic field. *Journal of Geophysical Research*, *115*(E11).

Williams, Q. (2009). Bottom-up versus top-down solidification of the cores of small solar system bodies: Constraints on paradoxical cores. *Earth and Planetary Science Letters*, *284*(3), 564-569. doi: 10.1016/j.epsl.2009.05.019

Wilson, A. J., Alfè, D., Walker, A. M., & Davies, C. J. (2023). Can homogeneous nucleation resolve the inner core nucleation paradox? *Earth and Planetary Science Letters*, *614*, 118176.

Wilson, A. J., Walker, A. M., Alfè, D., & Davies, C. J. (2021). Probing the nucleation of iron in earth's core using molecular dynamics simulations of supercooled liquids. *Phys. Rev. B*, *103*(21), 214113.